Novel Quasi-Resonant Parameter Optimization Method of LCC–LCC Compensated IPT Systems With Wide Output Range

Ke Shi, *Member, IEEE*, Chunsen Tang, *Member, IEEE*, Tianxu Feng, *Member, IEEE*, Peiyue Wang, Jincheng Jiang, Shuaiyong Li, *Senior Member, IEEE*, and Jie Hou, *Member, IEEE*

***Abstract*—In this article, a novel nonresonant *LCC–LCC* topology modeling and quasi-resonant parameter optimization method is proposed for inductive power transfer (IPT) systems. The new characteristics of nonresonant *LCC–LCC* topology are revealed and its modeling method using a variable resistor for battery load is presented. Wide-range power regulation is achieved directly through parameter configuration without additional circuit transformers, and the system maintains the zero-voltage switching (ZVS) condition with approximate constant current output characteristics. In addition, the lower limit for the detuning ratio coefficient and the widening of the detuning parameters selection are realized by magnetic integration design. Compared with existing traditional resonant parameter configuration methods, the proposed method aims to improve the overall performance of multiple working points within the quasi-resonant range, achieving a new effect of high ZVS robustness, wide parameter configuration range, and improved power transfer capability. The detailed design process of quasi-resonant parameters and integrated magnetic coupler are given. A 6.5-kW power level prototype is implemented to validate the proposed method. Experimental results show that within the designed quasi-resonant range, a 96.9% increase from 3.3 kW to 6.5 kW in output power is achieved under a constant proximity resonance state. The efficiency reaches 92.4% .**

***Index Terms*—Inductive power transfer (IPT), magnetic integration, nonresonant *LCC–LCC* topology, output power regulation, quasi-resonance.**

Received 12 March 2025; revised 16 June 2025; accepted 25 July 2025. Date of publication 29 July 2025; date of current version 8 September 2025. This work was supported in part by the Municipal Education Commission Science and Technology Research Plan Project of Chongqing under Grant KJQN202400626 and Grant KJZD-M202300605, in part by the National Natural Science Foundation of China under Grant 52307004, in part by the National Natural Science Foundation of China under Grant 62373070, in part by the Key Project of Chongqing Technological Innovation and Application Development under Grant CSTB2024TIAD-KPX0073, and in part by the Natural Science Foundation of Chongqing under Grant CSTB2024NSCQ-LZX0035 and Grant CSTB2024NSCQ-QCXMX0054. Recommended for publication by Associate Editor L. Corradini. *(Corresponding author: Ke Shi.)*

Ke Shi, Tianxu Feng, Peiyue Wang, Jincheng Jiang, Shuaiyong Li, and Jie Hou are with the School of Automation, Chongqing University of Posts and Telecommunications, Chongqing 400065, China (e-mail: shike@cqupt.edu.cn; fengtx@cqupt.edu.cn; wangpy@cqupt.edu.cn; jiangjinc@cqupt.edu.cn; lishuaiyong@cqupt.edu.cn; houjie@cqupt.edu.cn).

Chunsen Tang is with the School of Automation, Chongqing University, Chongqing 400000, China (e-mail: cstang@cqu.edu.cn).

Color versions of one or more figures in this article are available at https://doi.org/10.1109/TPEL.2025.3593649.

Digital Object Identifier 10.1109/TPEL.2025.3593649

I. Introduction

INDUCTIVE power transfer (IPT) technology enhances the flexibility and independence between ground power supply equipment and onboard receiving equipment, effectively overcoming problems such as cumbersome operation, exposed wires, and potential leakage risks in traditional wired charging modes. It has been applied to biomedical implants [1], consumer electronics [2], and electric vehicles [3]. Resonance compensation topology eliminates reactive power to improve power transmission capability and reduce circuit losses, a vital component of IPT systems [4]. Therefore, it is of significance to improve the resonant topology performance.

The *LCC–LCC* topology has been proven an ideal choice for battery-loaded IPT systems [5]. Improvements have been made to the performance of *LCC–LCC* topology from three aspects: tuning methods [6], [7], extra couplings optimization [8], [9], and composite topology optimization [10], [11]. In addition, the characteristics of *LCC–LCC* topology under nonresonant parameter configuration have also been proven to be a method for improving system performance, which become a research hotspot recently. In [12], the ZVS condition of the electric vehicle wireless charging system was realized through the parameter optimization design of compensation components, which is conducive to high efficiency. In [13], a parameter offline tuning method realized by switching the parallel-compensated capacitance for a detuned *LCC–LCC* resonant converter was proposed. In [14], an *LCC–LCC* topology with switch-controlled-capacitors topology was proposed to improve the misalignments tolerance for IPT systems. Two detuned parameters were controlled to match and tune to ensure the ZVS condition. These methods explored the characteristics of *LCC–LCC* topology under nonfully resonant parameter configuration in terms of antioffset and efficiency improvement. In [15], the latest load modeling methods for wireless power transfer systems have been summarized. In addition to the constant resistance model, the variable resistance model was adopted for S-S topologies to analyze the system characteristics under resonant parameter configuration. In [16], the rated power flow during coupling variations was achieved by frequency control at a constant voltage. In [17], a precise fundamental harmonic approximation was presented for modeling resonant S-S topologies with a variable resistance load. These studies focus on a certain

resonant working point using variable resistance models, optimized the IPT system through frequency control or precise modeling. However, the mechanism of the variable resistance model under nonresonant parameter configuration for *LCC–LCC* topology is still unclear.

Although the analysis focusing on discrete resonant working points provided important insights for *LCC–LCC* topology parameter optimization to a certain extent [18], [19], [20], [21], the limitations of previous research on the analysis of detuned *LCC–LCC* topology such as ZVS robustness, quasi-resonant range characteristics, power transmission capability still exist. For higher-order and more complex *LCC–LCC* topologies with battery loads, the equivalent load on the output side is also constrained by voltage, which cannot be reflected in the constant resistance load model. This characteristic is more significant for nonresonant parameter configuration. Therefore, the characteristics of *LCC–LCC* topology under nonresonant parameter configuration need further analysis.

This article proposes a novel quasi-resonant parameter optimization method of *LCC–LCC* topology with wide-range power regulation capability. The new characteristics of nonresonant *LCC–LCC* topology are revealed using a variable resistor for battery load, and the quasi-resonant conditions are derived based on it. The parameter optimization method for quasi-resonant *LCC–LCC* topology is presented, which achieves the ability to adjust the output power through a single parameter while maintaining customized ZVS conditions. The circuit parameter range corresponding to the quasi-resonant state is optimized through the magnetic integration method, and its detailed design process is provided. The new contributions are listed as follows.

1) A novel nonresonant *LCC–LCC* topology modeling method is proposed using a variable resistance load model under the battery voltage constraint condition. A universal nonresonant *LCC–LCC* topology model is developed, and the quasi-resonant conditions are derived based on this model.
2) The parameter optimization method for quasi-resonant *LCC–LCC* topology is proposed, achieving its output power capability improvement while maintaining an optimal weak inductive ZVS condition. The approach offers a low overhead solution for adjusting output power using a single parameter.
3) A secondary-side magnetic integration scheme is proposed, which optimizes the circuit parameter configuration range of quasi-resonant *LCC–LCC* topology while making the coupler more compact.
4) The flowchart for optimizing the parameters of the quasi-resonant *LCC–LCC* topology is presented, facilitating the step-by-step customization of resonance conditions, output performance, and parameter robustness to meet practical requirements.

The rest of this article is organized as follows. In Section II, the circuit principal analysis of quasi-resonance is revealed. In Section III, the parameters optimization and parameter range expanding methods are presented. In Section IV, the practical system is built and the effectiveness of the proposed method is verified. In Section V, the effect of the misalignment is analyzed and the technological innovation of the method is further emphasized. Finally, Section VI concludes this article.

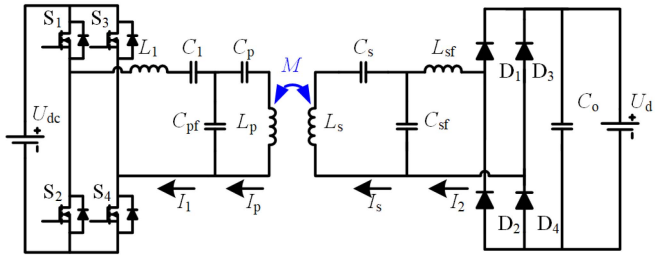

Fig. 1. Circuit of *LCC–LCC* topology with a battery load.

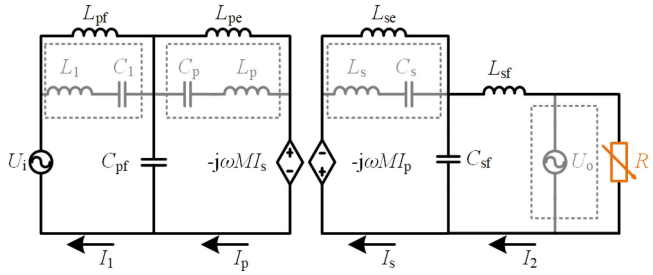

Fig. 2. Equivalent circuit of the *LCC–LCC* topology with a variable resistance load model.

II. Analysis of Quasi-Resonant LCC–LCC Topology

The double-side *LCC–LCC* topology with a battery load is shown in Fig. 1. The equivalent circuit of the *LCC–LCC* topology with the variable resistance model is shown in Fig. 2. S_1–S_4 are four power MOSFETs in the primary side. D_1–D_4 are the secondary-side rectifier diodes. L_p and L_s are the transmitting coil and the receiving coil. L_1, L_{sf}, C_1, C_{pf}, C_p, C_{sf}, and C_s are the compensation inductors and capacitors in the *LCC–LCC* topology. L_{pf} is the series equivalent of L_1 and C_1. C_o is the filtering capacitor. M is the mutual inductance between the main coupling coils. $\boldsymbol{U}_{dc}$ and $\boldsymbol{U}_d$ are the dc input and output voltage. $\boldsymbol{U}_i$ and $\boldsymbol{U}_o$ are the equivalent input and output voltage, respectively. $\boldsymbol{I}_1$ and $\boldsymbol{I}_p$ are the inverter current vector and the transmitting coil current vector. $\boldsymbol{I}_s$ and $\boldsymbol{I}_2$ are the receiving coil current vector and the output current vector.

The coupling coils and series compensation capacitor are equivalently as follows:

$$\omega^2 C_p(L_p - L_{pe}) = \omega^2 C_s(L_s - L_{se}) = 1. \tag{1}$$

The compensation capacitor C_{sf} is set as the detuning factor, and the detuning ratio coefficient is defined as h. The parameters are set as

$$\omega^2 L_{pf} C_{pf} = \omega^2 L_{pe} C_{pf} = h\omega^2 L_{se} C_{sf} = 1, L_{se} = L_{sf}. \tag{2}$$

The voltage of the battery load has a certain range, and the voltage does not change suddenly during charging, which can be considered as a constant voltage value for high-frequency IPT systems. Due to the constant voltage at the battery terminal and the filtering effect of the *LCC* resonant network, the input voltage of the rectifier bridge appears as a square wave while the

current approximates a fundamental sine wave. The combination of a rectifier and a constant voltage load behaves similarly to a linear resistor that consumes the actual power delivered to the battery at the fundamental frequency. The actual zero-crossing points of the input voltage and the input current align precisely in each half-cycle, as determined by the physical characteristics and fundamental operating principles of diodes. Hence, the fundamental components of voltage and current can be considered nearly in phase with each other. This means that the overall equivalent impedance of the rectifier bridge, filtering capacitor, and battery exhibits approximately pure resistance characteristics. The model that equates the battery, rectifier bridge, and filter capacitor as a constant ac resistor is widely used in wireless charging systems [22], [23], [24], [25], especially in the research and analysis of battery loads. These methods are effective and sufficient when the analysis is limited to specific operating points with resonant parameter design. But the constant resistance model cannot capture the various steady-state variations in equivalent resistance configuration with changes in internal parameters of the IPT system. Focus on nonresonant topology configuration conditions, the battery load with a rectifier circuit can be expressed as a variable resistor under the constraint of the battery voltage

$$\left|\dot{U}_o\right| = \left|\dot{I}_2\right| R. \tag{3}$$

The KVL equation of the system is expressed as

$$\begin{bmatrix} 0 & \mathrm{j}\omega L_{\mathrm{pf}} & 0 & 0 \\ \mathrm{j}\omega L_{\mathrm{pf}} & 0 & -\mathrm{j}\omega M & 0 \\ 0 & -\mathrm{j}\omega M & \mathrm{j}\omega(1-h)L_{\mathrm{se}} & \mathrm{j}\omega h L_{\mathrm{se}} \\ 0 & 0 & \mathrm{j}\omega h L_{\mathrm{se}} & \mathrm{j}\omega(1-h)L_{\mathrm{se}}+R \end{bmatrix} \cdot \begin{bmatrix} \dot{I}_1 \\ \dot{I}_{\mathrm{p}} \\ \dot{I}_{\mathrm{s}} \\ \dot{I}_2 \end{bmatrix} = \begin{bmatrix} \dot{U}_{\mathrm{i}} \\ 0 \\ 0 \\ 0 \end{bmatrix}. \tag{4}$$

First, solve the mathematical expression of vector $\boldsymbol{I}_2$ based on (4), and then combine it with the variable resistance load constraint condition in (3). In this way, the variable resistor can be converted into a description of the output voltage modulus.

By solving (4), the circuit currents are obtained as

$$\begin{cases} \dot{I}_1 = \frac{M^2\dot{U}_{\mathrm{i}}(R-\mathrm{j}(h-1)\omega L_{\mathrm{se}})}{\omega {L_{\mathrm{pf}}}^2 L_{\mathrm{se}}(-\mathrm{j}(h-1)R+(2h-1)\omega L_{\mathrm{se}})} \\ \dot{I}_{\mathrm{p}} = -\frac{\mathrm{j}\dot{U}_{\mathrm{i}}}{\omega L_{\mathrm{pf}}} \\ \dot{I}_{\mathrm{s}} = \frac{M\dot{U}_{\mathrm{i}}(R-\mathrm{j}(h-1)\omega L_{\mathrm{se}})}{\omega L_{\mathrm{pf}} L_{\mathrm{se}}(-\mathrm{j}(h-1)R+(2h-1)\omega L_{\mathrm{se}})} \\ \dot{I}_2 = \frac{hM\dot{U}_{\mathrm{i}}}{L_{\mathrm{pf}}((h-1)R+\mathrm{j}(2h-1)\omega L_{\mathrm{se}})}. \end{cases} \tag{5}$$

The modulus of the output current is obtained as

$$\left|\dot{I}_2\right| = \frac{hM\left|\dot{U}_{\mathrm{i}}\right|}{L_{\mathrm{pf}}\sqrt{(1-h)^2R^2+(1-2h)^2\omega^2{L^2}_{\mathrm{se}}}}. \tag{6}$$

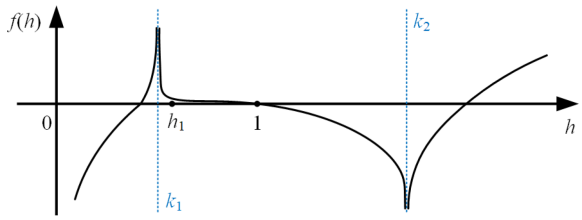

Fig. 3. Schematic curve of $f(h)$ with h.

By substituting (6) into (3), the variable resistance R is

$$R = \frac{(2h-1)\omega L_{\mathrm{pf}} L_{\mathrm{sf}}\left|\dot{U}_{\mathrm{o}}\right|}{\sqrt{\left|(h^2-2h+1){L^2}_{\mathrm{pf}}\left|\dot{U}_{\mathrm{o}}\right|^2 - h^2M^2\left|\dot{U}_{\mathrm{i}}\right|^2\right|}}. \tag{7}$$

Combine (6) and (7), the modulus of $\boldsymbol{I}_2$ is rewritten as

$$\left|\dot{I}_2\right| = \frac{hM\left|\dot{U}_{\mathrm{i}}\right|}{|2h-1|\,\omega L_{\mathrm{pf}} L_{\mathrm{se}}\sqrt{1+\frac{1}{\left|1-\frac{h^2}{(h-1)^2}\frac{M^2|\dot{U}_{\mathrm{i}}|^2}{{L^2}_{\mathrm{pf}}|\dot{U}_{\mathrm{o}}|^2}\right|}}}. \tag{8}$$

The total input equivalent impedance of the system is

$$Z_{\mathrm{in}} = \dot{U}_{\mathrm{i}}/\dot{I}_1. \tag{9}$$

The tangent value of the resonant angle directly quantifies the resonance phase deviation, and as a normalized numerical result, its comparability covers different design conditions. To enhance generality and better describe the degree of resonance deviation under different detuning parameters, the tangent angle is chosen as the indicator of weak inductive coupling. Combining (5), (7), and (9), it is expressed in (10), shown at the bottom of the next page. It can be concluded that $f(h)$ passes through point (10). And it has two boundary lines: $h = k_1 = L_{\mathrm{pf}}|\boldsymbol{U}_{\mathrm{o}}|/(L_{\mathrm{pf}}|\boldsymbol{U}_{\mathrm{o}}|+M|\boldsymbol{U}_{\mathrm{i}}|)$ and $h = k_2 = L_{\mathrm{pf}}|\boldsymbol{U}_{\mathrm{o}}|/(L_{\mathrm{pf}}|\boldsymbol{U}_{\mathrm{o}}|-M|\boldsymbol{U}_{\mathrm{i}}|)$. By optimizing the system parameter L_{pf}, a small function value close to zero is expected to be achieved within $(k_1,1)$, presented by the schematic curve of $f(h)$ in Fig. 3. The positive and negative values represent inductive and capacitive, respectively. Therefore, a weak inductive ZVS condition can be achieved within the range of h in $(h_1, 1)$ based on the demand for maximum deviation from the resonance state. And the maximum resonant angle tangent value within this range is

$$f(h)_{\max} = \frac{(h_1-1)\left(M^2\left|\dot{U}_{\mathrm{i}}\right|^2 - {L^2}_{\mathrm{pf}}\left|\dot{U}_{\mathrm{o}}\right|^2\right)}{L_{\mathrm{pf}}\left|\dot{U}_{\mathrm{o}}\right|\sqrt{{h_1}^2M^2\left|\dot{U}_{\mathrm{i}}\right|^2 - (h_1-1)^2{L^2}_{\mathrm{pf}}\left|\dot{U}_{\mathrm{o}}\right|^2}}. \tag{11}$$

According to (11), after the standard input and output voltages are determined, $f(h)_{\max}$ is a function expression of variables h_1, L_{pf}, and M.

The output power under resonance is defined as $P_{\mathrm{out}}|_{h\,=\,1}$ and the output power under detuning ratio coefficient h_1 is defined as $P_{\mathrm{out}}|_{h\,=\,h1}$. By combining (7) and (8), $P_{\mathrm{out}}|_{h\,=\,h1}$ can be solved as shown in (12), shown at the bottom of the next page.

In addition, taking $h = 1$ in (4), the standard output power under the resonant state is solved as

$$P_{\text{out}}|_{h=1} = \frac{M\left|\dot{U}_{\text{i}}\right|\left|\dot{U}_{\text{o}}\right|}{\omega L_{\text{pf}} L_{\text{ses0}}} \tag{13}$$

where L_{ses0} is the equivalent self-inductance value of the series branch on the secondary-side *LCC* topology, which is under the resonant configuration condition.

Then, the power regulation ratio γ is defined as

$$\gamma = \frac{P_{\text{out}}|_{h=h_1} - P_{\text{out}}|_{h=1}}{P_{\text{out}}|_{h=1}} \times 100\%. \tag{14}$$

Furthermore, the proposed variable resistance modeling method is limited to $h > k_1$ based on Fig. 3. After the standard mutual inductance value of the IPT system is ensured, under the objectives of maximum resonant angle tangent $f(h)_{\max}$ and power regulation ratio γ, the lower limit of the quasi-resonant range h_1 can be obtained by (11) and (14).

The range (h_1, 1) is defined as quasi-resonant parameter range. Within it, based on (8), an approximately constant current output characteristic can be realized through reasonable parameter settings. From (11), the weak inductive ZVS condition of the entire quasi-resonant range can be ensured by designing a smaller $f(h)_{\max}$ close to zero. And different values of h within the range correspond to different output powers, providing a novel access to power regulation. In addition, based on (10), different output voltages exert a slight influence on the tangent value of the resonant angle within a specific range, considering the limits of battery charging voltages range. This will not alter the fundamental principles of the proposed quasi-resonant configuration, which will be validated in the experiments presented in Section IV. By optimizing the system parameters effectively, an improvement in output power capability can be achieved while preserving the optimal weak inductive ZVS condition within the quasi-resonant range.

III. Parameter Optimization and Rang Expansion Based on Magnetic Integration

A. Optimization of the Quasi-Resonant Parameters

In practical applications, the sizes of the transmitting and receiving coils are subject to various restrictions based on the purpose, environment, and structure. The structures of the transmitting coil, receiving coil, and integrated inductor coil are selected as single polarity square coils as an example. And the parameters of the initial coupler are selected under a 6.5-kW power level example system. The operating frequency is $f =$ 85 kHz. The amplitude of $\boldsymbol{U}_{\text{i}}$ and $\boldsymbol{U}_{\text{o}}$ are both 200 V. At the transmitter, the size of the transmitting coil is designed as "450 mm × 450 mm × 5 mm". The turns N_{p} is designed as 7. At the receiver, the size of the receiving coil is designed as "300 mm × 300 mm × 5 mm". The turns N_{s} is designed as 10. The ferrite plate and aluminum shield of the same size with coils are used on both sides for magnetic field enhancement and electromagnetic shielding, respectively. The transfer distance is $d = 100$ mm. The measured mutual inductance is $M = 13.7$ μH.

The expected power regulation ratio and maximum resonant offset are set in advance as two design goals. Then, the quasi-resonant range and the compensation parameters are optimized based on the system standard mutual inductance. In this article, to verify the feasibility of the proposed method, the expected power regulation ratio is set to $p = 0.95$, and the expected maximum resonant angle tangent offset value is set to $q = 0.03$. The flowchart for the optimization of the circuit parameters is shown in Fig. 4. In the optimization process, the parameters of the initial system are first determined and the standard mutual inductance is analyzed. Next, solve the optimized h_1 and L_{pf} based on the equations: $f(h)_{\max} = q$, $\gamma = p$. Then, based on the standard output power requirement under resonant state in (13), the self-inductance value L_{ses0} of the series branch on the secondary side of the *LCC* topology is solved.

Based on the initial parameters, the design process of optimizing quasi-resonant parameters is carried out, resulting in $L_{\text{pf}} = 14$ μH, $L_{\text{ses0}} = 18.6$ μH and $h_1 = 0.65$. Under optimized parameter, the optimized quasi-resonant range is (0.65, 1). To verify the superiority of the variable resistance modeling method for nonresonant *LCC–LCC* topology, a comparative analysis is conducted. Combine with (4) and (9), the resonant angle tangent obtained from solving the conventional IPT system with a constant resistance model is

$$\tan\beta = g(h) = \frac{(1-h)[(1-2h)\omega^2 L^2{}_{\text{se}} + R^2]}{h^2 \omega L_{\text{se}} R}. \tag{15}$$

$$\tan\alpha = \frac{\text{Im}[Z_{\text{in}}]}{\text{Re}[Z_{\text{in}}]} = f(h) = \frac{(h-1)\left((1-2h)L^2{}_{\text{pf}}\left|\dot{U}_{\text{o}}\right|^2 + \left|h^2M^2\left|\dot{U}_{\text{i}}\right| - (h-1)^2L^2{}_{\text{pf}}\left|\dot{U}_{\text{o}}\right|^2\right|\right)}{h^2 L_{\text{pf}}\left|\dot{U}_{\text{o}}\right|\sqrt{\left|h^2M^2\left|\dot{U}_{\text{i}}\right|^2 - (h-1)^2L^2{}_{\text{pf}}\left|\dot{U}_{\text{o}}\right|^2\right|}} \tag{10}$$

$$P_{\text{out}}|_{h=h_1} = \left|\dot{I}_2\right|^2 R = \frac{h_1{}^2M^2\left|\dot{U}_{\text{i}}\right|^2\left|\dot{U}_{\text{o}}\right|\sqrt{\left|h_1{}^2M^2\left|\dot{U}_{\text{i}}\right|^2 - (-1+h_1)^2L_{\text{pf}}{}^2\left|\dot{U}_{\text{o}}\right|^2\right|}}{(-1+2h_1)\,\omega L_{\text{pf}}L_{\text{se}}\left[(-1+h_1)^2L_{\text{pf}}{}^2\left|\dot{U}_{\text{o}}\right|^2 + \left|h_1{}^2M^2\left|\dot{U}_{\text{i}}\right|^2 - (-1+h_1)^2L_{\text{pf}}{}^2\left|\dot{U}_{\text{o}}\right|^2\right|\right]} \tag{12}$$

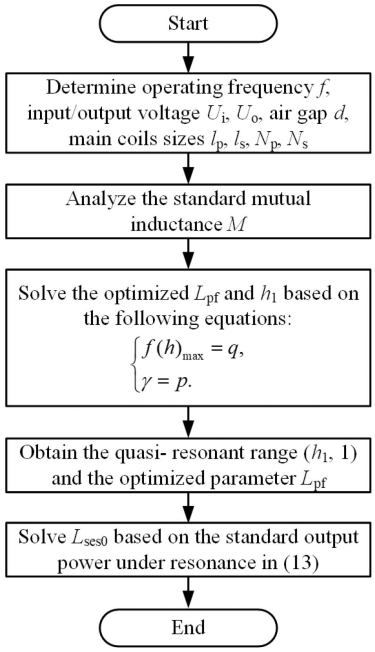

Fig. 4. Flowchart for the design of quasi-resonant parameter, where q is the expected maximum resonant angle tangent offset value, p is the expected power regulation ratio.

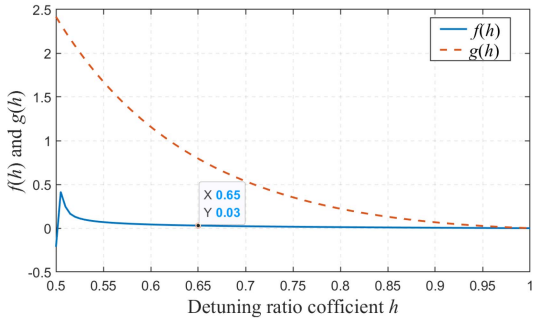

Fig. 5. Function curves of $f(h)$ and $g(h)$ with h under optimized parameters.

Based on the standard output power under resonant configuration, the equivalent resistance of the load R is set to 12 Ω. The function curves of $f(h)$ and $g(h)$ with the detuning ratio coefficient h under the optimized parameter configuration are plotted in Fig. 5. The calculation results show that the parameter optimization results obtained by using the modeling method in this article can achieve a larger range of detuning ratio coefficients under good ZVS conditions.

B. Parameter Range Expanding by Magnetic Integration

1) Principles of Magnetic Integration Design: The proposed circuit analysis method is universal to nonresonant *LCC–LCC* topology. Based on the initial magnetic coupler, a typical secondary side unipolar magnetic integrated structure is configurated. The windings of the secondary-side coils are in the same direction. The cross mutual inductance between the integrated coil and the transmitting coil M_{psf} can be designed small enough to be negligible compared with the main mutual inductance. M_{sf} is the internal mutual inductance between the integrated coil and the receiving coil, which can be equivalent to a T-type network. Based on the physical essence of mutual inductance decoupling, the magnetic coupling effect can be transformed into a series-parallel relationship of pure inductance, achieving circuit equivalence [8], [26], [27]. The equivalent circuit with the T-type network of the internal mutual inductance M_{sf} is shown in Fig. 6. The L_{se} in the previous theoretical analysis is replaced with $L_{ses} = L_{se}+M_{sf}$. The change in L_{se} value caused by it does not affect the analysis in Section II since the resonant angle in (10) is independent of L_{se}. In addition, according to (8), the magnetic integration brings a fixed proportional multiple of output current, which does not affect the analysis of approximate constant current output characteristics. Therefore, theoretical analysis in Section II is applicable for the internal coupled magnetic integration. According to (2), the original h is

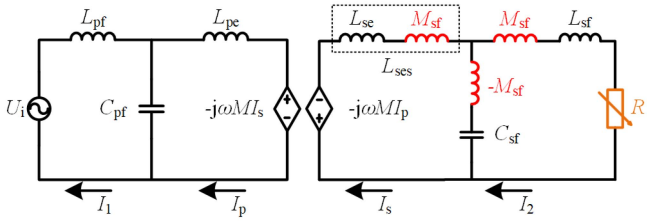

Fig. 6. Equivalent circuit with the T-type network of the internal mutual inductance M_{sf}.

$$h = \frac{1}{C_{sf}} \cdot \frac{1}{\omega^2 L_{sf}}. \tag{16}$$

Under the effect of M_{sf}, the parameter h' is represented as

$$h' = \frac{M_{sf}}{L_{sf}+M_{sf}} + \frac{1}{C_{sf}} \cdot \frac{1}{\omega^2(L_{sf}+M_{sf})} \geq \frac{M_{sf}}{L_{sf}+M_{sf}}. \tag{17}$$

Comparing (16) and (17), two characteristics from M_{sf} can be obtained. First, the selection of circuit parameters C_{sf} corresponding to the quasi-resonant range is broadened. Parameters h and h' are both proportional functions of $1/C_{sf}$. In (17), the proportionality coefficient is $1/[\omega^2(L_{sf}+M_{sf})]$, which is smaller than $1/(\omega^2 L_{sf})$ in (16). Therefore, h' has a smaller change rate along with the change of C_{sf}. The selection of C_{sf} is broadened corresponding to the same range of the variable h'. The parameter sensitivity is greatly reduced and the fault tolerance rate is improved. Second, a fixed lower limit of detuning ratio coefficient is introduced, which can be used as a design index to configure the range of the detuning circuit parameter. In both (16) and (17), the detuning ratio coefficients are negatively correlated with C_{sf}. Within the concerned h range of (01), as C_{sf} increases, the lower limit of h is zero. In contrast, the lower limit of h' is $M_{sf}/(L_{sf}+M_{sf})$, a positive value that can be configured through system parameters. Therefore, the magnetic integration brings a detuning ratio coefficient lower limit, and the setting of the lower limit decides the degree of circuit parameters broadening. The selection of the circuit parameter corresponding to the quasi-resonant range can be designed by configuring the lower limit of the detuning ratio coefficient. In this way, sensitivities of the detuning circuit parameter can be configured. Through a secondary-side magnetic integration,

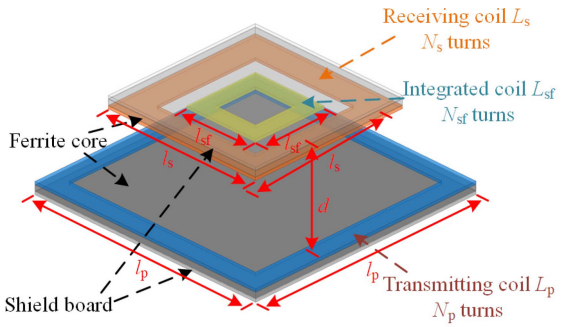

Fig. 7. Structures and dimensions of the coupler.

TABLE I
PARAMETERS OF THE MAGNETIC COUPLER

Type	Parameter	Description
Initial parameters	l_p	Length of L_p
	l_s	Length of L_s
	N_p	Turns of L_p
	N_s	Turns of L_s
	d	Transfer distance
Optimization parameters	l_{sf}	Length of L_{sf}
	N_{sf}	Turns of L_{sf}

the lower limit configuration of the detuning ratio coefficient is realized while making the coupler more compact. The range of circuit parameters corresponding to the quasi-resonance range is also broadened, which makes the quasi-resonate optimization method proposed in this article more practically applicable.

2) Optimization of the Coupler: The magnetic coupler structure is shown in Fig. 7. The parameters describing the coupler dimensions are defined in Table I. The equivalent inductance in the secondary-side resonant network is L_{ses}, which is the superposition of L_{sf} and M_{sf}. The flowchart for the optimization of the coupler is shown in Fig. 8. In this article, the lower limit of the set detuning ratio coefficient is $g = 1/3$. In this way, according to (16) and (17), the change rate of the detuning ratio coefficient with $1/C_{sf}$ can be reduced to two-thirds of its original value. Thus, a wider range of selection for the detuned circuit parameter C_{sf} can be achieved, and parameter sensitivity can be reduced. As shown in Fig. 4, L_{ses0} is the expected theoretical value calculated according to the standard power level demand under resonance. It serves as the key target for designing the secondary-side integrated inductor coil. To facilitate the convergence of finite element analysis and take into account the inherent manufacturing tolerances of coils, the judgment condition of inductance value L_{ses} is set as $0.97L_{ses0} \leq L_{ses} \leq 1.03L_{ses0}$ ($\pm 3\%$ tolerance range). M_{psf} may have adverse effects on the resonance state and efficiency of the system, which needs to be alleviated by adding a constraint objective. Therefore, the expected upper limit of cross inductance is set to 0.1, which means that M_{psf} can be almost ignored relative to M. In this way, the impact of M_{psf} on the circuit can be ignored, which is one of our design goals. The AWG38 Lize wire diameter is $a = 5$ mm, and the step size of the integrated coil length is $\Delta l_{sf} = 10$ mm. First, analyze the self-inductance

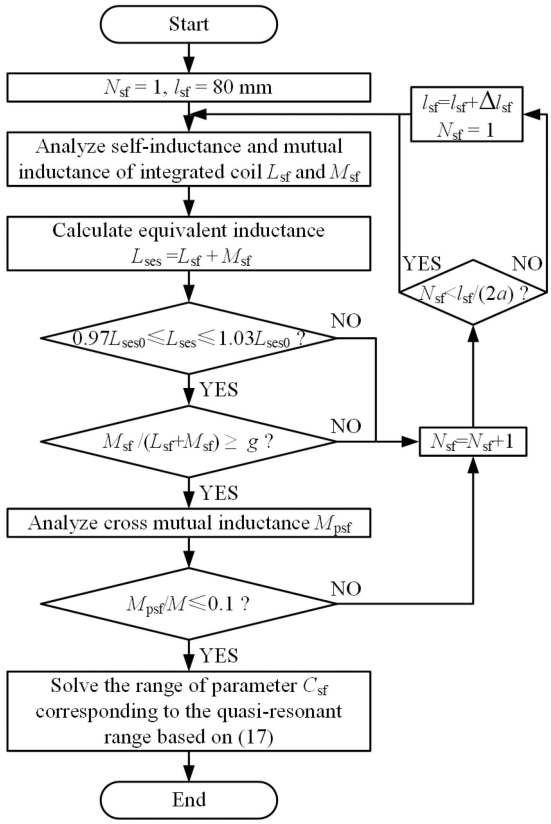

Fig. 8. Flowchart for the design of the coupler, where a and Δl_{sf} are the diameter of litz wire and step size of integrated coil length l_{sf}. g is the lower limit of the detuning ratio coefficient configuration.

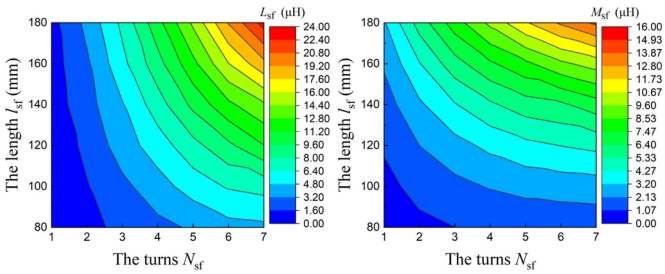

Fig. 9. Results of the inductance L_{sf} and the inner mutual inductance M_{sf} with the turns N_{sf} and the length l_{sf}.

and the internal mutual inductance of the integrated inductor coil. Calculate the equivalent inductance L_{ses}. Second, optimize the side length and the turns of the integrated inductor coil based on the expected inductance value L_{ses0}, constrained by the lower limit of the detuning ratio coefficient and the cross mutual inductance ratio. Finally, solve the range of detuning circuit parameter C_{sf} corresponding to the quasi-resonant range based on (17).

The expected equivalent inductance value L_{ses0} calculated under the resonant condition is the primary design objective. The lower limit of the detuning ratio coefficient and the cross-inductance ratio are two constraint conditions. Focusing on the optimization design of N_{sf} and l_{sf}, the results of the inductance L_{sf}, and the inner mutual inductance M_{sf} are shown in Fig. 9. In

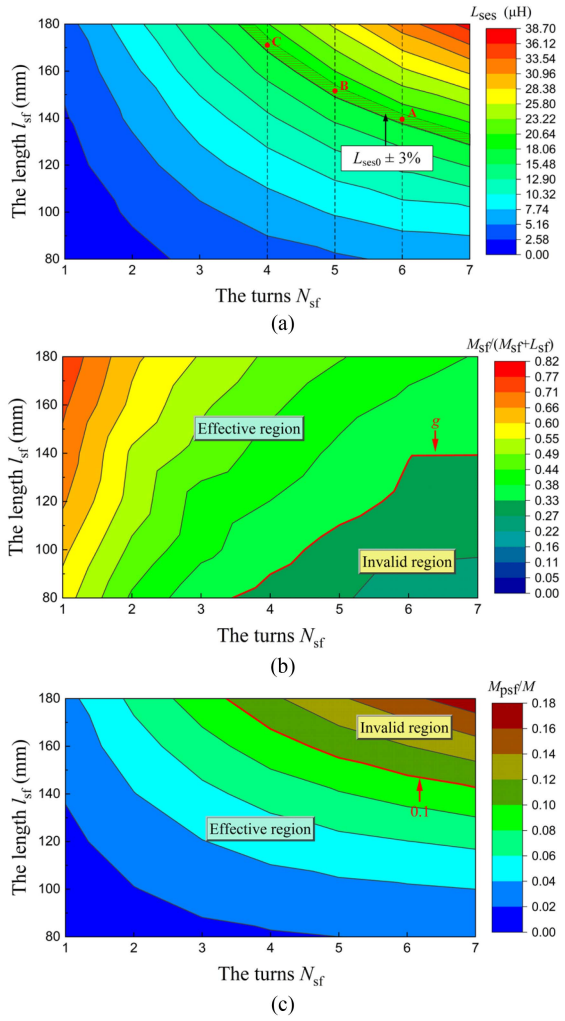

Fig. 10. Design process of the secondary-side integrated inductor coil turns N_{sf} and length l_{sf}. (a) Under the demand of the expected equivalent inductance L_{ses0}. (b) Under the demand of the lower limit of the detuning ratio coefficient configuration. (c) Under the demand of the cross-mutual inductance ratio.

the design process, the judgment condition of $0.97L_{ses0} \leq L_{ses} \leq 1.03L_{ses0}$ is the most important optimization step. To achieve the optimal condition, a finite element analysis is conducted. Select the range of side length l_{sf} and choose an appropriate range of turns within the constraints of the internal geometry size of the receiving coil. As shown in Fig. 8, the side length is used as the first optimization variable to traverse, and the turns are used as the subsequent optimization variable. Through electromagnetic simulations of the system, the inductance and mutual inductance for each combination of N_{sf} and l_{sf} is calculated. Therefore, as shown in Fig. 10(a), after the first judgment, three optimization result combinations will be obtained in sequence, namely A: 140 mm with 6, B: 150 mm with 5, and C: 170 mm with 4. The lower limit of the corresponding detuning ratio coefficient and the cross-coupling ratio calculated are shown in Fig. 10(b) and Fig. 10(c), respectively. The shaded areas are invalid regions, and the parameters within these ranges do not meet the corresponding expected criteria. The first result satisfies both constraints simultaneously. Therefore, according to the logic of the design

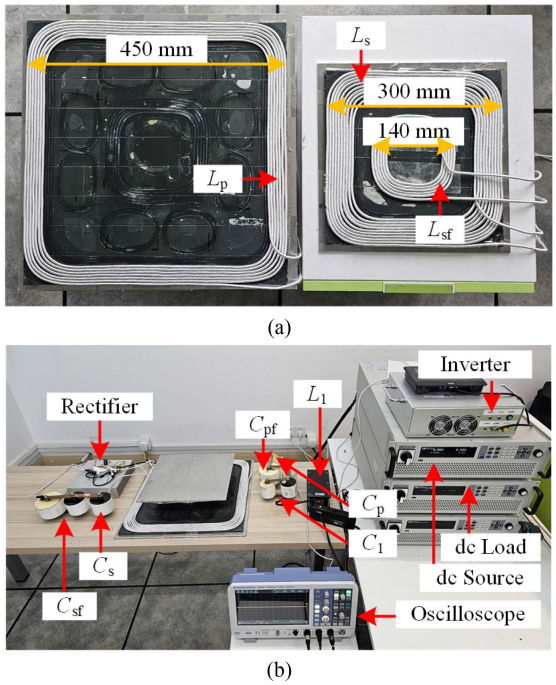

Fig. 11. Prototype of the IPT system. (a) Magnetic coupler with integrated coil. (b) Experimental platform.

process in Fig. 8, the optimization result is 140 mm with 6. Therefore, the size of the secondary-side integrated inductor coil is designed as "140 mm × 140 mm × 5 mm". The turns N_{sf} is designed as 6.

According to the detailed flowchart for optimizing the parameters of the quasi-resonant *LCC–LCC* topology, the customized configuration of the resonance state, output performance, and parameter robustness can be easily designed step-by-step under addressing practical requirements.

IV. Experimental Validation

A. Experimental Setup and Results

To verify the results of theoretical analysis and design methods, the experimental coils wound according to the design results in Section III are shown in Fig. 11(a). The overall experimental prototype is constructed as shown in Fig. 11(b).

At the input, a dc source and a high-power inverter are used to provide 200 V ac excitation for the resonant circuit. CREE silicon-carbide MOSFETs (C2M0025120D) with 25 mΩ internal resistance are adopted by the inverter. The PWM control signal for the MOSFET is generated by the control chip TMS320F28335. The output is a fixed frequency of 85 kHz. At the output, CREE C3D20060D diodes are used for the rectifier to provide dc current to the EA-CPS-8080 electronic load. The electronic load is set to constant voltage mode with 200 V. The coils are made from 1000-strand AWG 38 Litz-wire. The magnetic material PC95 is used to construct the ferrite board. The measured parameters of the coupler and the calculated parameters are shown in Table II. M_{psf} is approximately 1.2 μH, much smaller than the M of

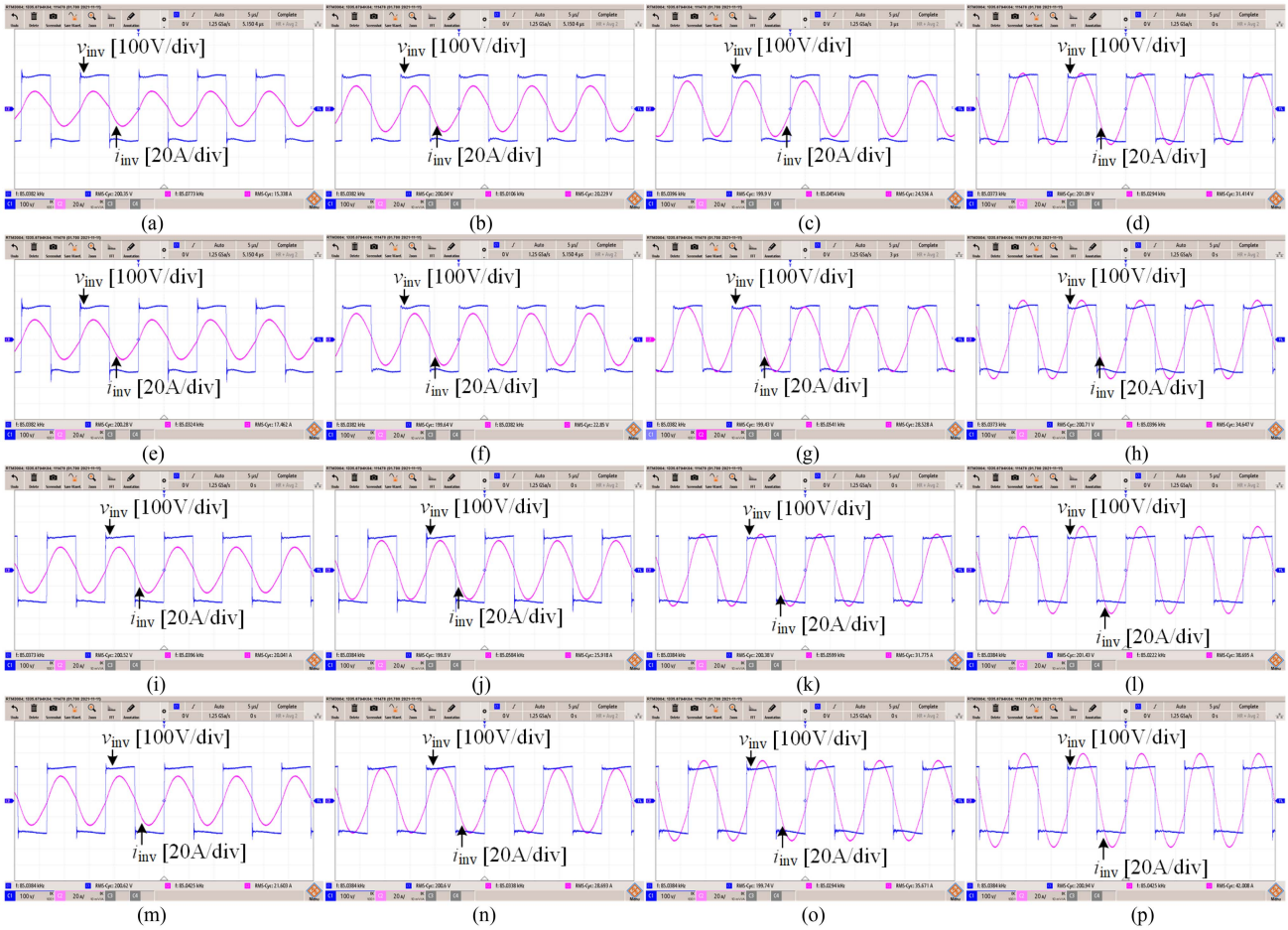

Fig. 12. Steady waveforms of the inverter voltages and currents at different quasi-resonant points (C_{sf}, h) under output voltages of 175 V, 200 V, 225 V, and 250 V. (a) $C_{sf} = 285$ nF ($h = 1$), $U_o = 175$ V. (b) $C_{sf} = 400$ nF ($h = 0.81$), $U_o = 175$ V. (c) $C_{sf} = 500$ nF ($h = 0.71$), $U_o = 175$ V. (d) $C_{sf} = 600$ nF ($h = 0.65$), $U_o = 175$ V. (e) $C_{sf} = 285$ nF ($h = 1$), $U_o = 200$ V. (f) $C_{sf} = 400$ nF ($h = 0.81$), $U_o = 200$ V. (g) $C_{sf} = 500$ nF ($h = 0.71$), $U_o = 200$ V. (h) $C_{sf} = 600$ nF ($h = 0.65$), $U_o = 200$ V. (i) $C_{sf} = 285$ nF ($h = 1$), $U_o = 225$ V. (j) $C_{sf} = 400$ nF ($h = 0.81$), $U_o = 225$ V. (k) $C_{sf} = 500$ nF ($h = 0.71$), $U_o = 225$ V. (l) $C_{sf} = 600$ nF ($h = 0.65$), $U_o = 225$ V. (m) $C_{sf} = 285$ nF ($h = 1$), $U_o = 250$ V. (n) $C_{sf} = 400$ nF ($h = 0.81$), $U_o = 250$ V. (o) $C_{sf} = 500$ nF ($h = 0.71$), $U_o = 250$ V. (p) $C_{sf} = 600$ nF ($h = 0.65$), $U_o = 250$ V.

TABLE II
MEASURED PARAMETERS OF THE MAGNETIC COUPLER

Parameter	Value	Parameter	Value
L_1	42 μH	C_p	64.4 nF
L_p	67.1 μH	C_s	60.7 nF
L_s	70.0 μH	M	13.7 μH
L_{sf}	12.3 μH	M_{sf}	6.2 μH
C_{pf}	250 nF	M_{psf}	1.2 μH
C_1	125 nF	C_o	20 μF

13.7 μH. $M_{psf}/M = 0.08$, which means that the impact of M_{psf} on the system is negligible.

The tested charging voltage range is selected as 175 V–250 V, sufficient to meet the battery charging range [28], [29]. Fig. 12 shows the inverter output waveforms at different quasi-resonant points (C_{sf}, h) under output voltages of 175 V, 200 V, 225 V, and 250 V. v_{inv} is the inverter voltage and i_{inv} is the inverter current. The results indicate that at a standard output voltage of 200 V, the resonant angle varies relatively little within the entire quasi-resonant parameter range, and the inverter is in a good ZVS condition. In addition to the designed standard output voltage of 200 V, experimental tests are also performed at output voltages of 175 V, 225 V, and 250 V. The results indicate that within the range of quasi-resonant parameters under the output voltage of 175 V, the working point is closer to the fully resonant state than that under the standard output voltage of 200 V. It remains relatively stable, and the ZVS condition can still be achieved under variations of the detuning ratio coefficient. Under output voltages of 225 V and 250 V, within the range of quasi-resonant parameters, a decrease in the detuning ratio coefficient leads to a slight increase in the inductive degree beyond the designed resonant angle. But it still maintains fine weak inductive ZVS condition. Overall, the experiment verifies that the system can work efficiently within the optimized quasi-resonant parameter range, with the inverter sustaining an ideal slight inductive ZVS condition.

At the deviation point $C_{sf} = 600$ nF ($h = 0.65$), the output currents at different quasi-resonant point (C_{sf}, h) under output voltages of 175 V, 200 V, 225 V, and 250 V are shown in Fig. 13. Within the tested output voltage range, the maximum deviation of the output current from the standard value is 4%, indicating that an approximately constant current output is achieved within the optimized quasi-resonant range.

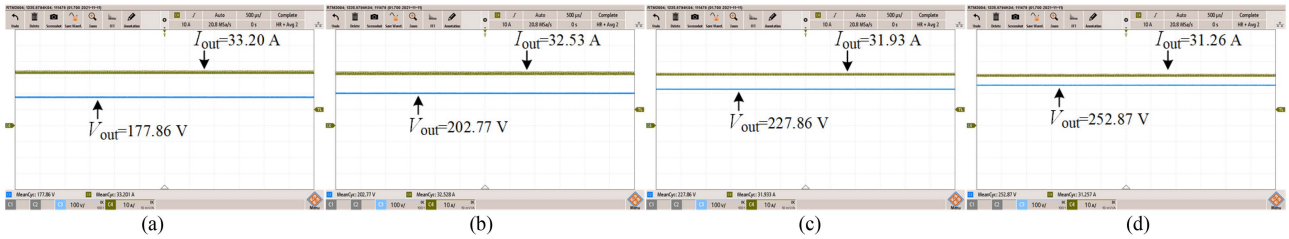

Fig. 13. Output currents at the deviation point $C_{sf} = 600$ nF ($h = 0.65$) under output voltages of 175 V, 200 V, 225 V, and 250 V. (a) $U_o = 175$ V. (b) $U_o = 200$ V. (c) $U_o = 225$ V. (d) $U_o = 250$ V.

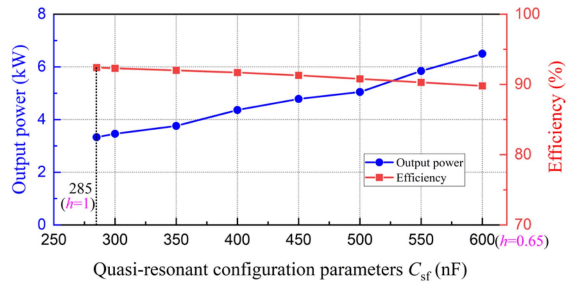

Fig. 14. Output power and efficiency within quasi-resonant working range.

Fig. 14 shows the output power and dc–dc overall system efficiency of the IPT system at different quasi-resonant points (C_{sf}, h) under the standard output voltage 200 V. Within the quasi-resonant range of (0.65, 1), the output power ranges from 3.3 kW to 6.5 kW. The output power regulation rate reaches 96.9% . And the dc–dc efficiency is from 89.8% to 92.4% . Although efficiency has slightly decreased, the system still operates within an acceptable and relatively high range. The results demonstrate that the proposed method achieves wide-range output power regulation while maintaining high efficiency in a near-resonant working condition.

B. Power Loss Analysis

Fig. 15 shows the power loss distributions at different quasi-resonant points under the standard output voltage of 200 V. The ferrite core loss is hard to detect, so the transmitter and receiver equivalent series resistance (ESR) are used to approximately evaluate the ferrite core loss. The power losses of the transmitter, the receiver, and the *LCC–LCC* compensation network are calculated by the component's ESR and current. The power losses of the inverter and the rectifier are calculated according to [30].

Overall, as the detuning ratio coefficient h decreases, there is a slight change in the distribution of the system losses. The proportion of transmitter loss decreased from 30.1% in Fig. 15(a) to 9.9% in Fig. 15(d), and the receiver loss increased from 19.5% in Fig. 15(a) to 26.7% in Fig. 15(d). This is caused by the proposed method changing the impedance relationship between the transmitter and receiver. The proportion of losses in other components has increased slightly, with rectifier bridge losses accounting for a relatively large proportion. In addition, although integrating the secondary-side compensation inductor

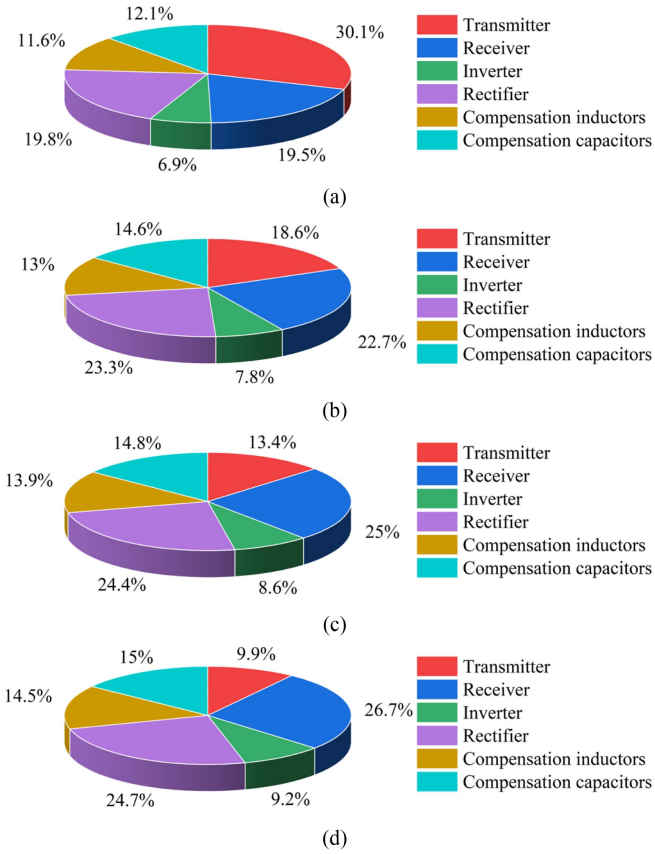

Fig. 15. Power loss distribution at different quasi-resonant points under the standard output voltage of 200 V. (a) $C_{sf} = 285$ nF ($h = 1$). (b) $C_{sf} = 400$ nF ($h = 0.81$). (c) $C_{sf} = 500$ nF ($h = 0.71$). (d) $C_{sf} = 600$ nF ($h = 0.65$).

as a coil within the magnetic coupler theoretically increases its internal resistance, the results show that the associated power loss proportion remains low. This is because the secondary-side integrated inductor coil introduces the internal mutual inductance M_{sf}, which increases the equivalent series inductance value of the secondary-side *LCC* topology. This means that the integrated inductor requires smaller self-inductance values compared to using external compensating inductors to achieve the same impedance.

The results indicate that the major loss is coil loss under the proposed design method, which is consistent with most IPT systems [31], [32], [33], [34], [35]. To further improve the performance of the proposed method, the expected maximum

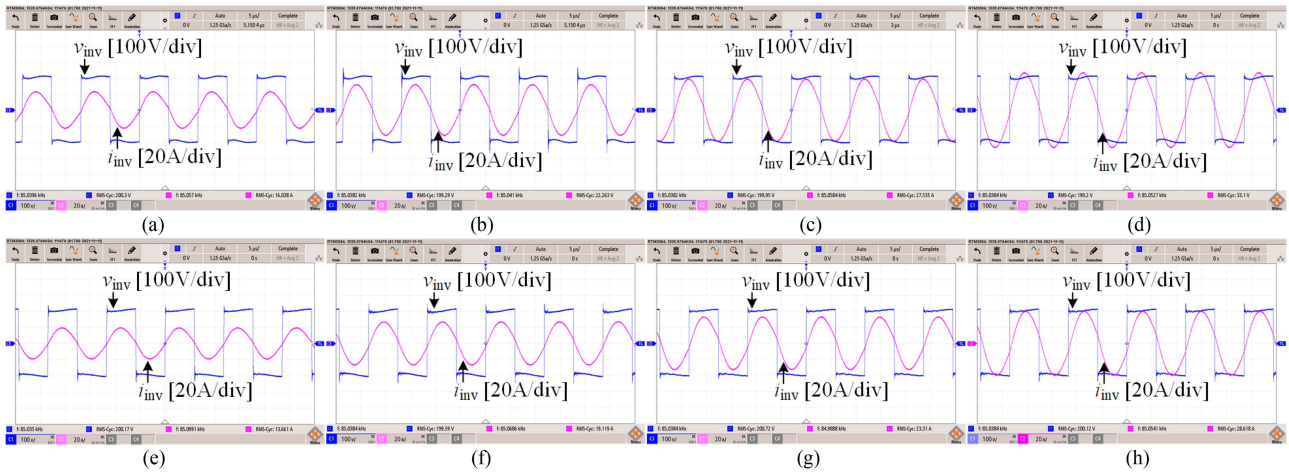

Fig. 16. Output voltages and currents at different quasi-resonant points (C_{sf}, h) under 5-cm and 10-cm horizontal misalignment, with standard input and output voltages. (a) $C_{sf} = 285$ nF ($h = 1$), 5-cm misalignment. (b) $C_{sf} = 400$ nF ($h = 0.81$), 5-cm misalignment. (c) $C_{sf} = 500$ nF ($h = 0.71$), 5-cm misalignment. (d) $C_{sf} = 600$ nF ($h = 0.65$), 5-cm misalignment. (e) $C_{sf} = 285$ nF ($h = 1$), 10-cm misalignment. (f) $C_{sf} = 400$ nF ($h = 0.81$), 10-cm misalignment. (g) $C_{sf} = 500$ nF ($h = 0.71$), 10-cm misalignment. (h) $C_{sf} = 600$ nF ($h = 0.65$), 10-cm misalignment.

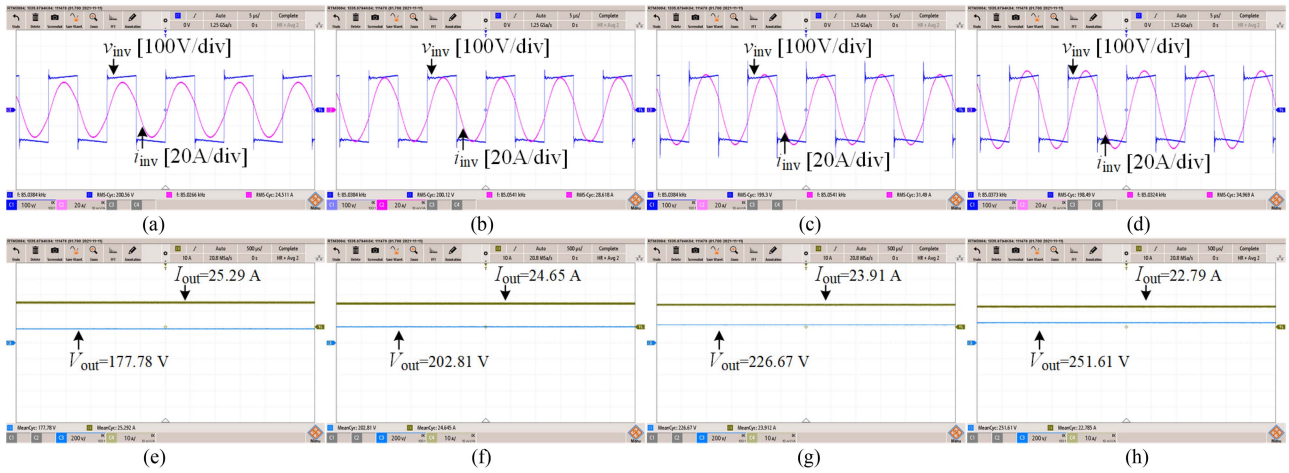

Fig. 17. Experimental results at the quasi-resonant point (600 nF, 0.65) under different output voltages with 10-cm misalignment. (a) Inverter output under $U_o = 175$ V. (b) Inverter output under $U_o = 200$ V. (c) Inverter output under $U_o = 225$ V. (d) Inverter output under $U_o = 250$ V. (e) Output current under $U_o = 175$ V. (f) Output current under $U_o = 200$ V. (g) Output current under $U_o = 225$ V. (h) Output current under $U_o = 250$ V.

resonant angle tangent offset value can be set small enough. When designing the main magnetic coupler, it is possible to consider configuring a smaller transmitting impedance and a larger receiving impedance to achieve a more balanced distribution of coil losses throughout the quasi-resonant range. Additionally, using larger-diameter Litz wires, low-loss magnetic cores, and smaller air gaps helps increase coupling coefficients, which reduces coil losses. To further reduce rectifier bridge losses, synchronous rectification can be implemented in future work.

V. Discussion

A. Discussion of Misalignment Tolerance

In this article, the analysis and optimization of parameter design mainly focus on the initial well-aligned mutual inductance. Mutual inductance decreases with the coupler misalignment, resulting in a slight shift of the resonant state towards the inductive region according to the calculation in (10). Furthermore, considering practical application scenarios, the impact of coupler misalignment is also investigated. Fig. 16 shows the inverter output voltage and current at different quasi-resonant points (C_{sf}, h) under standard input and output voltages with 5-cm and 10-cm horizontal misalignment. The results indicate that the quasi-resonant characteristics are less affected with a 5-cm horizontal misalignment. When the horizontal misalignment is 10 cm, the system working point shifts toward the inductive region, a trend that becomes more pronounced as h decreases. But even at the quasi-resonant edge ($h = 0.65$), the maximum tangent value of the resonant angle reaches 0.25 corresponding to 15°, which remains a good ZVS condition. Furthermore, to validate the robustness of the ZVS condition under different loads and misalignments, the detuning parameter configuration farthest from the resonant point is selected for testing. Fig. 17 shows the experimental results at the maximum detuning point

TABLE III
COMPARISON BETWEEN THE LATEST RELATED RESEARCH AND THIS WORK

Ref	Maximum efficiency	Output power	Topology	Modeling of battery load	Range of detuning ratio coefficient	Detuned parameters	Robustness to ZVS	Method
[13]	94.0%	6.1 kW	LCC-LCC	Constant resistance	α (1.12, 1.5) 133.9% β (1.24, 1.5) 120.9%	Two	Good	Tuning method with variable frequency
[14]	88.3%	0.3 kW	LCC-LCC	Constant resistance	C_1 (93.4 nF, 121.6 nF) 130.1% C_{f1} (245 nF, 568 nF) 231.8%	Two	Poor	Tuning method with capacitance adjustment
[16]	92.0%	0.7 kW	S-S	Variable resistance	x_c =1.03 f (104 kHz, 137 kHz) 131.7%	Two	Good	Frequency control method for rated power
[17]	90.5%	0.03 kW	S-S	Variable resistance	/	/	/	Modified FHA with high-order harmonics
This work	**92.4%**	**6.5 kW**	**LCC-LCC**	**Variable resistance**	***h* (0.65, 1) 153.8%**	**One**	**Good**	**Parameter optimization for quasi-resonant range**

(600 nF, 0.65) under different output voltages with a 10-cm misalignment. The results indicate that acceptable ZVS conditions are still achieved under different output voltages at a 10-cm misalignment for the maximum detuning ratio coefficient configuration within the quasi-resonant range. In addition, the maximum deviation between the output current and the standard value is 7%, which can generally be considered a relatively constant current characteristic for IPT systems. Therefore, under the tested 10-cm misalignment, a suitable ZVS condition can be achieved within the designed quasi-resonant range with the output voltage range of 175 V to 250 V, sufficient to meet practical requirements.

Within a certain range of coupler misalignment and output voltage variations, the system can still maintain ZVS conditions, accompanied by an improvement in wide-range output capability. In practical applications, the air gap distance, dead time of the inverter, magnetic coupler size, magnetic core configuration, parameter sensitivity capability, and ZVS design requirements need different suitable maximum resonant offset angles. In this article, to verify the feasibility of the proposed method, the expected maximum resonant angle tangent offset value q is set to 0.03. This is a relatively excellent parameter configuration choice, suitable for most IPT systems. Under various real-world application limitations and requirements, comprehensive parameters exhibiting corresponding quasi-resonant characteristics can be obtained based on the proposed method. When optimizing quasi-resonant parameters, the optimal, normal, and worst-situation scenarios of the actual system can be fully considered to determine the two design objectives needed to complete the corresponding parameter design and optimization. In practical applications, the maximum resonance deviation point may not be very close to the resonant state point. Different target parameters can be set according to varying needs in actual scenarios to obtain applicable quasi-resonant range parameter configurations.

B. Discussion of Advantages and Features

The proposed method employs a variable resistance model for the battery load to elucidate the quasi-resonant characteristics of the *LCC–LCC* topology. The efficient parameter configuration with a wide-range power regulation capability is optimized. The comparison between this article with the latest related research is given in Table III. The existing literature has studied dynamic tuning methods based on a constant resistance load model for *LCC–LCC* topology and frequency influence characteristics based on a variable resistance load model for S-S topology. The traditional methods were employed to optimize a certain discrete resonant working point. In contrast, the proposed method aims to optimize the quasi-resonant working range of *LCC–LCC* topology under nonresonant parameter configuration, achieving completely different effects. The characteristics of the quasi-resonant range are elucidated using a variable resistance model for the battery load. Based on the proposed method, the parameter design can be tailored to actual requirements, allowing for adjusting the output power at a relatively low cost. Meanwhile, the power transfer capability of the *LCC–LCC* topology has been further explored and improved. In summary, wide-range power regulation is achieved directly through parameter configuration without additional circuit transformers, and the system maintains the good ZVS condition with approximate constant current output characteristics. Regulating the output power while guaranteeing ZVS condition simultaneously only by tuning one parameter is realized. The resulting optimization effectively addresses the requirements of wireless charging.

A quasi-resonant parameter optimization method for *LCC–LCC* topology is proposed. This is a novel approach aimed at overcoming the limitations of previous research on the topology analysis of detuned *LCC–LCC* topologies, such as ZVS robustness, quasi-resonant range characteristics, and power transfer capability. The proposed parameter optimization method aimed at enhancing the overall system performance within the quasi-resonant range. In addition, the internal coupling between the secondary-side integrated coil and the receiving coil reduces the requirement for compensating inductance value under the same output power requirements. The actual required inductance value can be achieved with a smaller L_{sf}. Therefore, the integration of the secondary-side inductor results in a more compact coupler and contributes to improving power transmission performance.

The proposed method offers new insights into the performance analysis of the *LCC–LCC* topology under detuned configurations and provides novel, simple, and feasible solutions to enhance the output power capability of IPT systems.

VI. CONCLUSION

A quasi-resonant parameter optimization method for *LCC–LCC* topology is proposed, bringing the effect of adjusting the output power through a single parameter while maintaining customized ZVS conditions. The variable resistance model

for the battery load is presented to analyze the characteristics of nonresonant *LCC–LCC* topology. Based on the model, the quasi-resonant condition is designed according to the requirements of resonance offset and output power adjustment ratio. A lower limit for the detuning ratio coefficient and a broadening of the detuning circuit parameters selection are achieved by magnetic integration. An *LCC–LCC* topology with designed quasi-resonant parameters is taken as an example to show the superiority of the proposed method. The experimental results show that within the optimized quasi-resonant range (0.65, 1), the output power varies from 3.3 kW to 6.5 kW. Meanwhile, the weakly inductive ZVS condition is maintained. The system works efficiently, reaching a maximum of 92.4% .

REFERENCES

[1] S. Roy, A. N. M. W. Azad, S. Baidya, M. K. Alam, and F. Khan, "Powering solutions for biomedical sensors and implants inside the Human body: A comprehensive review on energy harvesting units, energy storage, and wireless power transfer techniques," *IEEE Trans. Power Electron.*, vol. 37, no. 10, pp. 12237–12263, Oct. 2022.

[2] J. Mai, X. Zeng, Y. Yao, Y. Wang, and D. Xu, "Improved winding and compensation methods for the multilayer coil in IPT system," *IEEE Trans. Ind. Electron.*, vol. 69, no. 5, pp. 5375–5380, May 2022.

[3] Y. Zhang et al., "Integration of onboard charger and wireless charging system for electric vehicles with shared coupler, compensation, and rectifier," *IEEE Trans. Ind. Electron.*, vol. 70, no. 7, pp. 7511–7514, Jul. 2023.

[4] W. Zhao, X. Qu, J. Lian, and C. K. Tse, "A Family of hybrid IPT couplers with high tolerance to pad misalignment," *IEEE Trans. Power Electron.*, vol. 37, no. 3, pp. 3617–3625, Mar. 2022.

[5] A. Khoshsaadat and J. S. Moghani, "Fifth-order T-type passive resonant tanks tailored for constant current resonant converters," *IEEE Trans. Circuits Syst. I, Reg. Papers.*, vol. 65, no. 2, pp. 842–853, Feb. 2018.

[6] Y. Chen et al., "A parameter tuning method for a double-sided compensated IPT system with constant-voltage output and efficiency optimization," *IEEE Trans. Power Electron.*, vol. 38, no. 3, pp. 4124–4139, Mar. 2023.

[7] Z. Luo, Y. Zhao, M. Xiong, X. Wei, and H. Dai, "A self-tuning LCC/LCC system based on switch-controlled capacitors for constant-power wireless electric vehicle charging," *IEEE Trans. Ind. Electron.*, vol. 70, no. 1, pp. 709–720, Jan. 2023.

[8] J. Wang, R. Chen, C. Cai, J. Zhang, and C. Wang, "An onboard magnetic integration-based WPT system for UAV misalignment-tolerant charging with constant current output," *IEEE Trans. Transport. Electron.*, vol. 9, no. 1, pp. 1973–1984, Mar. 2023.

[9] K. Shi, T. Feng, J. Jiang, P. Wang, Z. Meng, and C. Tang, "A highly magnetic integrated method of LCC-compensated IPT system with excellent misalignment tolerance," *IEEE Trans. Power Electron.*, vol. 38, no. 12, pp. 16256–16268, Dec. 2023.

[10] L. Zhao, D. J. Thrimawithana, U. K. Madawala, A. P. Hu, and C. C. Mi, "A misalignment-tolerant series-hybrid wireless EV charging system with integrated magnetics," *IEEE Trans. Power Electron.*, vol. 34, no. 2, pp. 1276–1285, Feb. 2019.

[11] Y. Zhang et al., "An integrated electric vehicle charging system of wireless power transfer and auxiliary power module with shared converter and magnetic coupler," *IEEE Trans. Ind. Electron.*, vol. 71, no. 9, pp. 10414–10421, Sep. 2024.

[12] F. Wang, W. Zhang, L. Ye, J. Guo, K. Liu, and H. T. Do, "A design method to implement ZVS for electric vehicle wireless charging system with double-side LCC compensation," *IEEE J. Emerg. Sel. Topics Power Electron.*, vol. 9, no. 3, pp. 3791–3801, Jun. 2021.

[13] J. Deng et al., "Frequency and parameter combined tuning method of LCC–LCC compensated resonant converter with wide coupling variation for EV wireless charger," *IEEE J. Emerg. Sel. Topics Power Electron.*, vol. 10, no. 1, pp. 956–968, Feb. 2022.

[14] X. Zhang, R. Xue, F. Wang, F. Xu, T. Chen, and Z. Chen, "Capacitor tuning of LCC-LCC compensated IPT system with constant-power output and large misalignments tolerance for electric vehicles," *IEEE Trans. Power Electron.*, vol. 38, no. 10, pp. 11928–11939, Oct. 2023.

[15] X. Wang, C. Q. Jiang, J. Zhou, L. Mo, and Y. Wang, "Enhanced modeling of wireless power transfer system with battery load," *IEEE Trans. Power Electron.*, vol. 39, no. 6, pp. 6574–6579, Jun. 2024.

[16] G. Guidi and J. A. Suul, "Minimizing converter requirements of inductive power transfer systems with constant voltage load and variable coupling conditions," *IEEE Trans. Ind. Electron.*, vol. 63, no. 11, pp. 6835–6844, Nov. 2016.

[17] A. Namadmalan, J. M. Alonso, and A. Iqbal, "Accurate fundamental harmonic modeling of inductive power transfer battery chargers," *IEEE Trans. Transport. Electron.*, vol. 8, no. 1, pp. 627–635, Mar. 2022.

[18] S. Luo, Z. Yao, Z. Zhang, X. Zhang, and H. Ma, "Balanced dual-side LCC compensation in IPT systems implementing unity power factor for wide load range and misalignment tolerance," *IEEE Trans. Ind. Electron.*, vol. 70, no. 8, pp. 7796–7809, Aug. 2023.

[19] Z. Sun, J. Sun, Y. Wang, and D. Xu, "An efficiency optimization method based on double side impedance angle design for wireless power transfer system," *IEEE Trans. Power Electron.*, vol. 38, no. 4, pp. 5000–5012, Apr. 2023.

[20] X. Li et al., "A high-efficiency IPT system with series-capacitor full-bridge configuration and inverse coupled current doubler rectifier for high-input, low-voltage, and high output current applications," *IEEE Trans. Power Electron.*, vol. 39, no. 9, pp. 11849–11861, Sep. 2024.

[21] F. Xu, S. Wei, J. Li, D. Yuan, and K. Chen, "Investigation on compensation topology and its parameter matching method for dynamic wireless power transfer system," *IEEE Trans. Ind. Appl.*, vol. 60, no. 4, pp. 5692–5701, Jul. 2024.

[22] W. Xiong et al., "A dual-frequency-detuning method for improving the coupling tolerance of wireless power transfer," *IEEE Trans. Power Electron.*, vol. 38, no. 6, pp. 6923–6928, Jun. 2023.

[23] Z. Chen, X. Sun, J. Liu, Y. Yan, J. Zhao, and B. Ren, "Output power control strategy for omnidirectional wireless power transfer system based on maximum mutual inductance information estimation," *IEEE J. Emerg. Sel. Topics Power Electron.*, vol. 12, no. 5, pp. 5383–5395, Oct. 2024.

[24] Y. Zhang, G. Wei, J. Zhang, L. Hao, and L. Cheng, "A hybrid topology relay based wireless power transfer system with mutual inductance enhancement and high misalignment tolerance," *IEEE Trans. Power Electron.*, vol. 40, no. 6, pp. 7640–7645, Jun. 2025.

[25] W. Zhou et al., "A secondary-side rotating and segmented capacitive power transfer system with low output voltage fluctuations based on three DC busbars," *IEEE J. Emerg. Sel. Topics Power Electron.*, to be published, doi: 10.1109/JESTPE.2024.3522288.

[26] J. Deng, W. Li, T. D. Nguyen, S. Li, and C. C. Mi, "Compact and efficient bipolar coupler for wireless power chargers: Design and analysis," *IEEE Trans. Power Electron.*, vol. 30, no. 11, pp. 6130–6140, Nov. 2015.

[27] N. Rasekh, J. Kavianpour, and M. Mirsalim, "A novel integration method for a bipolar receiver pad using LCC compensation topology for wireless power transfer," *IEEE Trans. Veh. Technol.*, vol. 67, no. 8, pp. 7419–7428, Aug. 2018.

[28] Y. Li et al., "Reconfigurable intermediate resonant circuit based WPT system with load-independent constant output current and voltage for charging battery," *IEEE Trans. Power Electron.*, vol. 34, no. 3, pp. 1988–1992, Mar. 2019.

[29] L. Wu, B. Zhang, and Y. Jiang, "A misalignment-tolerant autonomous wireless power transfer system for battery charging based on detuning control," *IEEE Trans. Power Electron.*, vol. 39, no. 3, pp. 3851–3863, Mar. 2024.

[30] B. X. Nguyen et al., "An efficiency optimization scheme for bidirectional inductive power transfer systems," *IEEE Trans. Power Electron.*, vol. 30, no. 11, pp. 6310–6319, Nov. 2015.

[31] T. Ma, C. Q. Jiang, C. Chen, Y. Wang, J. Geng, and C. K. Tse, "A low computational burden model predictive control for dynamic wireless charging," *IEEE Trans. Ind. Electron.*, vol. 71, no. 9, pp. 10402–10413, Sep. 2024.

[32] D. Wang, X. He, C. Fu, Q. Zhao, and Z. Zhang, "Dynamic wireless charging system for EVs with uniform voltage output based on flux pipe supply rail and H-type receiver," *IEEE J. Emerg. Sel. Topics Power Electron.*, to be published, doi: 10.1109/JESTPE.2024.3491858.

[33] C. Zhu et al., "A magnetic field concentration enhanced I-shaped transmitter for DWPT system to achieve low power fluctuation," *IEEE Trans. Power Electron.*, vol. 39, no. 1, pp. 1690–1700, Jan. 2024.

[34] T. Feng, K. Shi, J. Jiang, and P. Wang, "A solenoid magnetic coupler and its control method for omnidirectional wireless charging of UAVs," *IEEE Trans. Ind. Electron.*, vol. 72, no. 3, pp. 2540–2550, Mar. 2025.

[35] Y. Zhang, H. Zhou, R. Xie, X. Mao, X. Chen, and Z. Li, "A smooth-output dynamic wireless charging system for automated guided vehicles with dual-receiver magnetic coupler," *IEEE Trans. Power Electron.*, vol. 40, no. 4, pp. 4711–4715, Apr. 2025.

Ke Shi (Member, IEEE) received the B.E. degree in automation and Ph.D. degree in control theory and control engineering from the School of Automation, Chongqing University, Chongqing, China, in 2016, and 2022, respectively. He is currently a Lecturer with the School of Automation, Chongqing University of Posts and Telecommunications, Chongqing, China. His current research interests include wireless power transfer and power electronics, dynamic wireless charging systems, and magnetic integrated method.

Chunsen Tang (Member, IEEE) received the B.S. degree in automation and Ph.D. degree in control theory and control engineering from the School of Automation, Chongqing University, Chongqing, China, in 2004 and 2009, respectively.

In 2008, he was a Research Fellow with the Department of Electrical and Computer Engineering, The University of Auckland, Auckland, New Zealand. He was with the School of Automation, Chongqing University, Chongqing, in 2009 and he is currently a Professor. His current research interests include nonlinear modeling and analysis, intelligent control, and wireless power transfer.

Tianxu Feng (Member, IEEE) received the B.E. degree in automation and the Ph.D. degree in control theory and control engineering from the School of Automation, Chongqing University, Chongqing, China, in 2016 and 2022, respectively.

He is currently an Associate Professor with the School of Automation, Chongqing University of Posts and Telecommunications, Chongqing, China. His current research interests include the wireless power transfer and power electronics.

Peiyue Wang received the B.E. degree in automation from Xidian University, Xi'an, China, in 2015, and the Ph.D. degree in control theory and engineering from Chongqing University, Chongqing, China, in 2021.

He is currently a Lecturer with the School of Automation, Chongqing University of Posts and Telecommunications, Chongqing, China. His current research interests include the wireless power transfer and power electronics.

Jincheng Jiang received the Ph.D. degree in control theory and control engineering from the School of Automation, Chongqing University, Chongqing, China, in 2020.

He is currently a Lecturer with the School of Automation, Chongqing University of Posts and Telecommunications, Chongqing, China. His research interests include wireless power transfer technology and industrial IoT technology.

Shuaiyong Li (Senior Member, IEEE) received the B.Sc. degree in applied physics from the Xinyang Normal University, Xinyang, China, in 2010, and the Ph.D. degree in instrument science and technology from the Chongqing University, Chongqing, China, in 2014.

From 2021 to 2023, he was a Postdoctoral Fellow with the Chongqing University. He is currently a Full Professor with the School of Automation, Chongqing University of Posts and Telecommunications, Chongqing, China. He has authored and coauthored more than 60 scientific papers in international journals and conferences. His current research interests include simultaneous localization and mapping, mobile robot, fault diagnosis and remaining useful life prediction, defect detection and safety evaluation, and industrial Internet of things.

Jie Hou (Member, IEEE) received the B.Eng. degree in automation from North Minzu University, Yinchuan, China, in 2010, the M.Eng. degree in control science and engineering from Chongqing University, Chongqing, China, in 2013, and the Ph.D. degree in control theory and control engineering from the Dalian University of Technology, Dalian, China, in 2018.

From 2018 to 2021, he was a Lecturer with the Chongqing University of Posts and Telecommunications, Chongqing, where he is currently an Associate Professor. His current research interests include system identification and modeling.